Article

Ultrathin quantum light source with van der Waals $NbOCl_2$ crystal

https://doi.org/10.1038/s41586-022-05393-7

Received: 5 January 2022

Accepted: 28 September 2022

Published online: 4 January 2023

Check for updates

Qiangbing Guo[1,2,3,14]✉, Xiao-Zhuo Qi[4,5,14], Lishu Zhang[6,14], Meng Gao[7,14], Sanlue Hu[8], Wenju Zhou[9], Wenjie Zang[1], Xiaoxu Zhao[10], Junyong Wang[3,6], Bingmin Yan[9], Mingquan Xu[7], Yun-Kun Wu[4,5], Goki Eda[3,6], Zewen Xiao[8], Shengyuan A. Yang[11], Huiyang Gou[9], Yuan Ping Feng[3,6], Guang-Can Guo[4,5,12], Wu Zhou[7,13], Xi-Feng Ren[4,5,12]✉, Cheng-Wei Qiu[1,3]✉, Stephen J. Pennycook[2,7]✉ & Andrew T. S. Wee[3,6]✉

Interlayer electronic coupling in two-dimensional materials enables tunable and emergent properties by stacking engineering. However, it also results in significant evolution of electronic structures and attenuation of excitonic effects in two-dimensional semiconductors as exemplified by quickly degrading excitonic photoluminescence and optical nonlinearities in transition metal dichalcogenides when monolayers are stacked into van der Waals structures. Here we report a van der Waals crystal, niobium oxide dichloride ($NbOCl_2$), featuring vanishing interlayer electronic coupling and monolayer-like excitonic behaviour in the bulk form, along with a scalable second-harmonic generation intensity of up to three orders higher than that in monolayer WS_2. Notably, the strong second-order nonlinearity enables correlated parametric photon pair generation, through a spontaneous parametric down-conversion (SPDC) process, in flakes as thin as about 46 nm. To our knowledge, this is the first SPDC source unambiguously demonstrated in two-dimensional layered materials, and the thinnest SPDC source ever reported. Our work opens an avenue towards developing van der Waals material-based ultracompact on-chip SPDC sources as well as high-performance photon modulators in both classical and quantum optical technologies[1–4].

SPDC, a second-order nonlinear optical (NLO) process in which one photon is fissioned into a pair of correlated photons under energy and momentum conservation, lies at the core of quantum light sources for modern quantum technologies[1–4]. At present, SPDC-based quantum light sources are typically enabled by second-order NLO bulk crystals such as beta barium borate and lithium niobate ($LiNbO_3$)[3,4], which, however, are intrinsically disadvantageous for hybrid integrated quantum photonics on platforms that are compatible with complementary metal–oxide–semiconductor technology owing to their three-dimensional (3D) covalent bonding nature, in addition to the relatively weak nonlinearities. The 2D layered materials, with unique van der Waals structure, enable bond-free integration without lattice and processing limitations[5]. They also show enhanced many-body electronic effects and relaxed phase-matching conditions, leading to large optical nonlinearity at the 2D limit[6–9], and have therefore attracted intense interest for integrated NLO optoelectronics and photonics[1,5]. However, to our knowledge, no unambiguous evidence of any SPDC process has ever been observed in 2D layered materials, primarily owing to low second-order NLO conversion efficiencies in the layered materials reported so far[4,10,11].

On one hand, the nonlinear conversion efficiency is restricted by the vanishing light–matter interaction length due to the atomic thickness[6,8]. For example, the absolute light–matter interactions in monolayer transition metal dichalcogenides (TMDCs) are too weak for practical applications, despite their extremely large second-order susceptibility[6]. On the other hand, the nonlinear efficiency of many 2D layered materials is not scalable with thickness for two reasons, the first being the centrosymmetry variation with layer number[8,12]. Typically, TMDCs usually stack in the 2H polytype by alternate orientation of each monolayer along the *c* axis, thus only odd layers have nonzero $\chi^{(2)}$ under the electric dipole approximation[13,14]. This is also applicable to other 2D materials including hexagonal BN, group IV monochalcogenides[15], $PdSe_2$ (ref. [16]) and $AgInP_2S_6$ (ref. [15]). The second reason is the significantly modified electronic structure due to strong interlayer

[1]Department of Electrical and Computer Engineering, National University of Singapore, Singapore, Singapore. [2]Department of Materials Science and Engineering, National University of Singapore, Singapore, Singapore. [3]Centre for Advanced 2D Materials and Graphene Research Centre, National University of Singapore, Singapore, Singapore. [4]CAS Key Laboratory of Quantum Information, University of Science and Technology of China, Hefei, China. [5]CAS Center for Excellence in Quantum Information and Quantum Physics, University of Science and Technology of China, Hefei, China. [6]Department of Physics, National University of Singapore, Singapore, Singapore. [7]School of Physical Sciences and CAS Key Laboratory of Vacuum Physics, University of Chinese Academy of Sciences, Beijing, China. [8]Wuhan National Laboratory for Optoelectronics, Huazhong University of Science and Technology, Wuhan, China. [9]Center for High Pressure Science and Technology Advanced Research, Beijing, China. [10]School of Materials Science and Engineering, Peking University, Beijing, China. [11]Research Laboratory for Quantum Materials, Singapore University of Technology and Design, Singapore, Singapore. [12]Hefei National Laboratory, University of Science and Technology of China, Hefei, China. [13]CAS Center for Excellence in Topological Quantum Computation, University of Chinese Academy of Sciences, Beijing, China. [14]These authors contributed equally: Qiangbing Guo, Xiao-Zhuo Qi, Lishu Zhang, Meng Gao. ✉e-mail: qbguo90@hotmail.com; renxf@ustc.edu.cn; chengwei.qiu@nus.edu.sg; stephen.pennycook@cantab.net; phyweets@nus.edu.sg

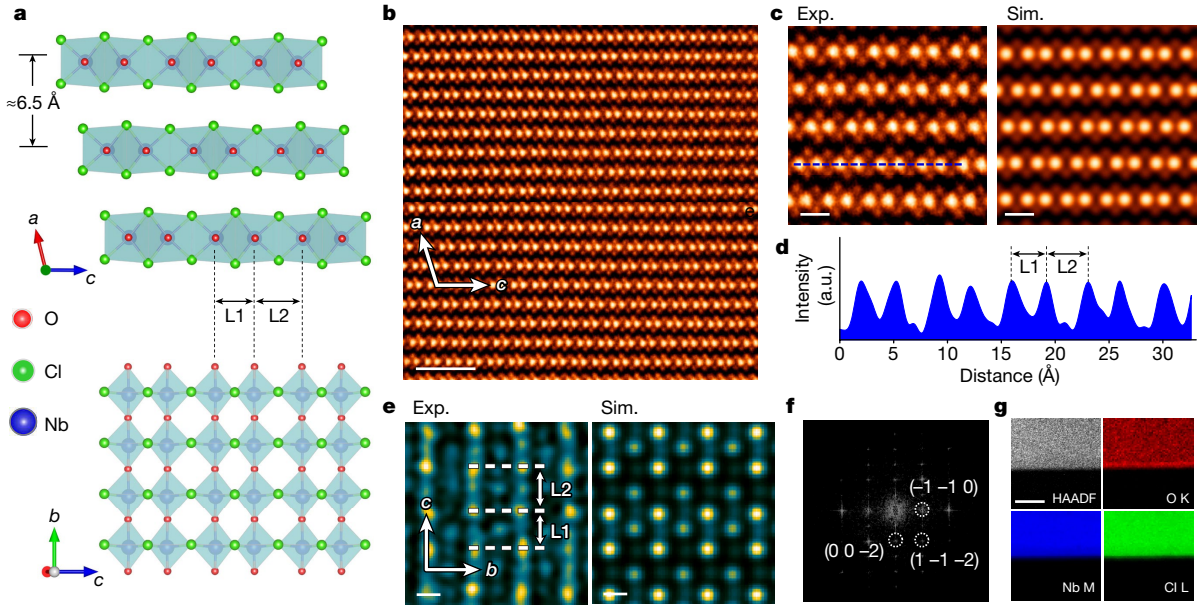

Fig. 1 | Structural characterization. a, Out-of-plane (top) and in-plane (bottom) representations of the crystal structure of $NbOCl_2$. The thickness of a single layer is about 6.5 Å. $NbOCl_2$ crystallizes in the *C*2 space group, in which Nb atoms show a 1D Peierls distortion, inducing a polarization along the *b* axis and two alternating unequal Nb–Nb distances (that is, L1 ≠ L2) along the *c* axis. **b**,**c**, Cross-sectional atomic-resolution ADF-STEM images of the crystal viewed along the *b* axis (**b**,**c** left (Exp., experimental)) and the corresponding simulated (Sim.) image (**c** right). Scale bars, 2 nm (**b**) and 0.5 nm (**c**). **d**, Line intensity profile along the *c* axis in **c** (blue dashed line), showing the alternating unequal Nb–Nb distances. a.u., arbitrary units. **e**, An in-plane atomic-resolution ADF-STEM image (left) and the corresponding simulated image (right) of the crystal. Scale bars, 0.2 nm. **f**, Fast Fourier transform pattern obtained from a typical in-plane ADF-STEM image. **g**, A high-angle annular dark-field (HAADF) image of a flake and the corresponding EELS elemental mapping images. Scale bar, 50 nm.

electronic coupling and dielectric screening that leads to decreased nonlinearity in addition to the self-absorption effects[12–18], such as in TMDC odd layers[12–14], α-In_2Se_3 (ref. [18]) and 3R-MoS_2 (refs. [8,15]).

Therefore, a van der Waals crystal with a scalable second-order NLO response is highly desirable, especially for the rapidly developing hybrid integrated photonic platforms in which facile van der Waals integration will facilitate unprecedented technology opportunities[1,5,19,20]. Here we report a van der Waals crystal, $NbOCl_2$, that features vanishing interlayer electronic coupling and a considerable monolayer-like excitonic effect, strong structural polarity and anisotropy, as well as a scalable and strong second-harmonic generation (SHG) response of up to three orders of magnitude greater than that in monolayer WS_2. The giant classical second-order nonlinearity stimulates us to explore its quantum counterparts providing the quantum–classical correspondence[10]. Nonclassical parametric photon pair generation through the SPDC process was unambiguously observed in flakes as thin as about 46 nm, with a figure of merit for SPDC efficiency as large as 9,800 GHz W^{-1} m^{-1}, holding great potential for constructing chip-integrated SPDC sources[10,21]. Our work demonstrates $NbOCl_2$ as a giant second-order NLO van der Waals crystal with great potential for applications in both classical and quantum nonlinear optical systems.

Crystal characterization

$NbOCl_2$ crystallizes in the *C*2 space group[22,23] with a van der Waals stacking behaviour along the *a* axis (Fig. 1a,b and Supplementary Fig. 1) and an interlayer distance of about 0.65 nm. Nb atoms exhibit a 1D Peierls distortion[23], resulting in a polarization along the *b* axis and two alternating unequal Nb–Nb distances (that is, L1 ≠ L2) along the *c* axis (Fig. 1a), which can be directly observed by atomic-resolved annular dark-field scanning transmission electron microscopy (ADF-STEM) and confirmed by the corresponding simulated images (Fig. 1c–e and Supplementary Fig. 3), in which alternate Nb–Nb distances can be clearly identified (Fig. 1d,e). The single-crystalline nature was further checked and collaboratively confirmed by X-ray diffraction (Supplementary Fig. 2), fast Fourier transform pattern analysis (Fig. 1f) and electron energy-loss spectroscopy (EELS) mapping images (Fig. 1g and Supplementary Fig. 4). Notably, $NbOCl_2$ crystals can be easily exfoliated by the normal mechanical exfoliation method. Monolayer and few-layer flakes are regularly obtained as well as large rectangular thin flakes (lateral size up to 10^2 μm) with sharp edges (Supplementary Fig. 5), indicative of weak interlayer interaction and strong intralayer crystallographic anisotropy. The exfoliated flakes are stable under ambient conditions with no obvious change in 2 weeks (Supplementary Figs. 6 and 7).

Vanishing interlayer electronic coupling

The layer-dependent electronic structures were characterized by STEM-based valence EELS, which is a powerful tool for studying optical excitations in nanostructures with ultrahigh spatial and energy resolutions[24]. Figure 2a shows the normalized EELS results for different layers, in which we can see that the optical excitation starts from around 1.6 eV (see enlargements in Fig. 2b) but remains at a low intensity up to 3 eV. Significant optical excitation appears only after 3 eV and comes to its first peak at around 4 eV. It is interesting to note that the optical excitation onset energy for different layers exhibits almost no energy shift (experimental energy resolution of 0.021 eV); that is, it is insensitive to thickness (or layer number; Fig. 2b and Supplementary Fig. 8). As seen from Fig. 2c and Supplementary Table 1, this is in stark contrast with other typical 2D layered materials, especially TMDCs and black phosphorus whose bandgaps evolve significantly with layer number owing to considerable interlayer coupling[25,26].

The weak evolution of the onset optical excitation is supported by the electronic structure calculations. The Heyd–Scuseria–Ernzerhof hybrid functional method[27] was first adopted for the calculation (detailed results are presented in Supplementary Fig. 9, and compared in Fig. 2c), which shows a very weak bandgap evolution from the monolayer (1.99 eV) to the bulk (1.98 eV) form along with a dispersionless

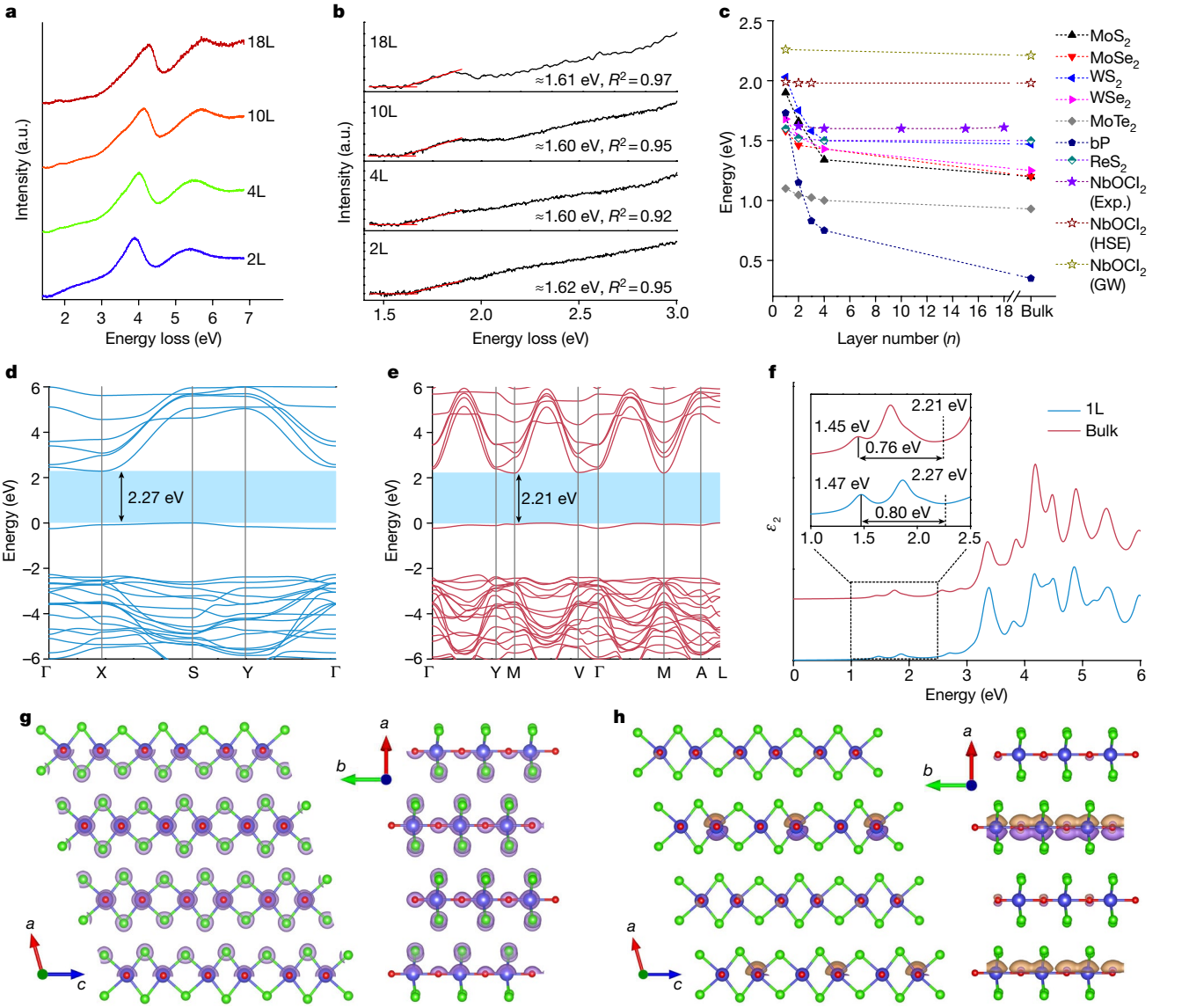

Fig. 2 | Weak interlayer electronic coupling. a, STEM-based valence EELS results for $NbOCl_2$ flakes of different thicknesses. The curves are normalized and an offset along the *y* axis is adopted for each curve for clarity. **b**, Corresponding enlargements of the onset region in **a**, which are fitted by a tangent method to derive an onset energy as indicated. **c**, Comparison of bandgap evolution with thickness among typical 2D layered materials. Detailed information can be found in Supplementary Table 1. A quite weak bandgap evolution in $NbOCl_2$ can be seen from both theoretical calculations and experimental results, compared with other typical layered materials. bP, black phosphorus; HSE, Heyd–Scuseria–Ernzerhof. **d**,**e**, Calculated quasiparticle band structures within the *GW* approximation for the monolayer (**d**) and bulk (**e**) forms. More details can be found in the Methods. **f**, Calculated optical absorption spectra for the monolayer and bulk forms by the method combining the *GW* approximation and the Bethe–Salpeter equation (see Methods). The inset shows an enlargement of the energy range between 1.0 and 2.5 eV, in which exciton binding energies of 0.8 eV for the monolayer form and 0.76 eV for the bulk form are derived. **g**, Interlayer charge density with an isosurface of 0.2 electrons per cubic bohr. **h**, Interlayer differential charge density with an isosurface of 0.0007 electrons per cubic bohr. This is calculated through assembling the bulk system from isolated monolayers, demonstrating a charge redistribution process. Yellow and purple colour denote depleted and accumulated charge density, respectively. Both **g** and **h** show that charge mainly distributes in the intralayer region, illustrating a negligible electronic wavefunction overlap between layers.

valence band maximum. The large discrepancy between the calculated bandgap value and the experimental optical excitation onset energy (EELS data), along with the indication of localized electrons (flat valence band maximum), stimulated us to include many-body effects in the calculation. First-principles calculation within the *GW* approximation was further used to reveal the electronic structures. As shown in Fig. 2d,e, the calculated quasiparticle bandgap values for the monolayer (2.27 eV) and the bulk (2.21 eV) form are also very close (also presented in Fig. 2c for comparison), which, together with the results of the Heyd–Scuseria–Ernzerhof calculations, indicates a weak interlayer electronic coupling.

The calculations using *GW* approximation and the Bethe–Salpeter equation (see details in Methods) unveil a considerable excitonic effect in both the monolayer and bulk forms, with a high exciton binding energy of about 0.8 eV for the monolayer form and about 0.76 eV for the bulk form. The calculated optical absorption onset at about 1.5 eV for both the monolayer and bulk forms is consistent with both experimental EELS and optical absorption data (Supplementary Fig. 10), indicating a necessity of considering excitonic effects.

It is noteworthy that both the quasiparticle bandgap and exciton binding energy are insensitive to layer number, revealing that a monolayer-like and considerable excitonic behaviour survived in the

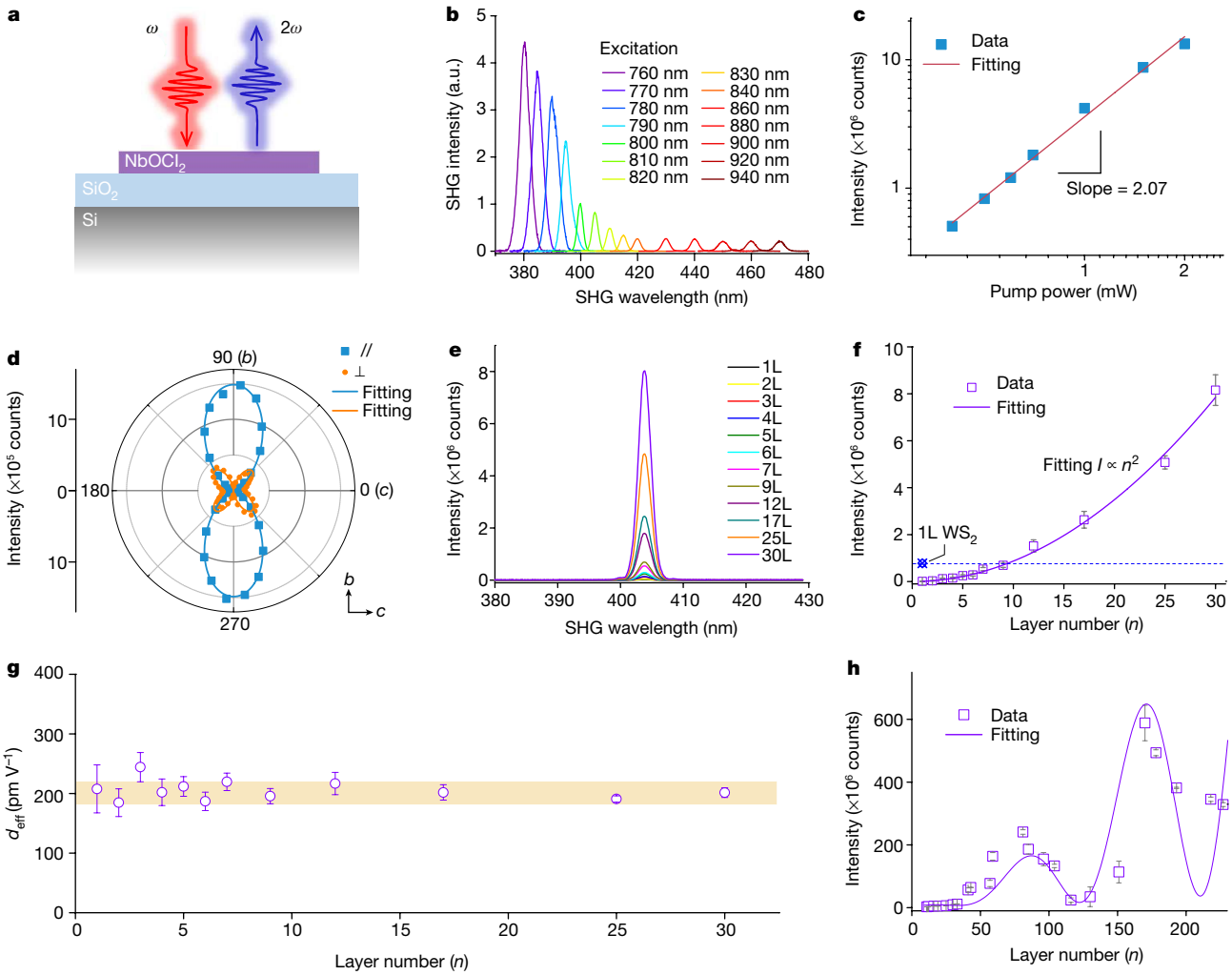

Fig. 3 | Anisotropic and scalable SHG response. a, Illustration of the measurement geometry. **b**, SHG spectra at different excitation wavelengths. **c**, Typical pump-power-dependent SHG intensity, which can be linearly fitted with a slope of 2.07, indicating the quadratic nature of the nonlinear optical process. **d**, Polarization-dependent SHG, indicating a highly anisotropic SHG response. **e**,**f**, SHG spectra of layers with different thicknesses (**e**) and the corresponding thickness-dependent SHG intensity (**f**) when pumped at 808 nm. SHG intensity scales with layer number in a manner that can be well fitted by a square function as indicated in **f**. The SHG intensity of monolayer WS_2 under the same condition is also presented for comparison. **g**, Thickness-dependent effective second-order nonlinear coefficient. The yellow shaded area indicates that the data points fall into a narrow range around 200 pm V^{-1}. **h**, Thickness-dependent SHG intensity in a broader thickness range (beyond the coherence length) where interference effects will take on a role, and peaks and dips can be observed when further scaling with thickness. Error bars represent standard deviations from multiple measurements.

bulk crystal. This is in sharp contrast to excitons in other 2D layered materials represented by TMDCs in which significant excitonic effects exist only in monolayers. The considerable monolayer-like excitonic effect in the bulk form, in turn, also evidences the weak interlayer electronic coupling as well as the weak dielectric screening effect in the cross-plane direction (Supplementary Fig. 11) in this unique layered crystal. The dispersionless valence band, resulting from the structural Peierls distortion (see detailed illustrations in Supplementary Fig. 12), denotes highly localized electronic states and contributes to the large exciton binding energy[28]. It is noted that the relatively weak optical absorption around the exciton and quasiparticle energies is attributed to the very localized Nb *4d* orbitals in the valence band maximum that contribute little to optical excitation (details can be found in Supplementary Fig. 13).

To unveil a more thorough picture of the weak interlayer electronic coupling, we calculated the interlayer charge density, as shown in Fig. 2g (see Supplementary Fig. 14 for more details). The electrons are mainly localized in the intralayer (mostly on Nb and O atoms; Supplementary Fig. 14) with negligible distribution in the interlayer region, implying mainly in-plane bonding. This can be further evidenced by the interlayer differential charge density (Fig. 2h) that is calculated by assembling the bulk system from isolated monolayers and reveals a charge redistribution process during interlayer coupling[26]. In addition, a negligible charge redistribution can be found in the interlayer region, indicating almost no covalency in the out-of-plane direction. By contrast, significant charge distribution can be found in the interlayer region of TMDCs and black phosphorus due to stronger interlayer bonding[25,26]. This rather weak interlayer coupling character in $NbOCl_2$ can be understood as follows. After grabbing an electron from the Nb atom, the *p* shell of the Cl atom is complete and becomes inert. Consequently, the interlayer interaction (bonding) is weak as Nb and O atoms are sandwiched by Cl atoms. The ionic bond of Nb–Cl is different from the Mo–S bond in MoS_2, which is, for example, more covalent[26]. Therefore, the strong ionicity of Nb–Cl bonds together with the structural Peierls distortion led to the extremely weak interlayer electronic coupling in $NbOCl_2$.

To gain further insights into the weak interlayer interactions, we also calculated and compared the interlayer binding energy, cleavage energy and translation energy, all of which reveal relatively low levels compared

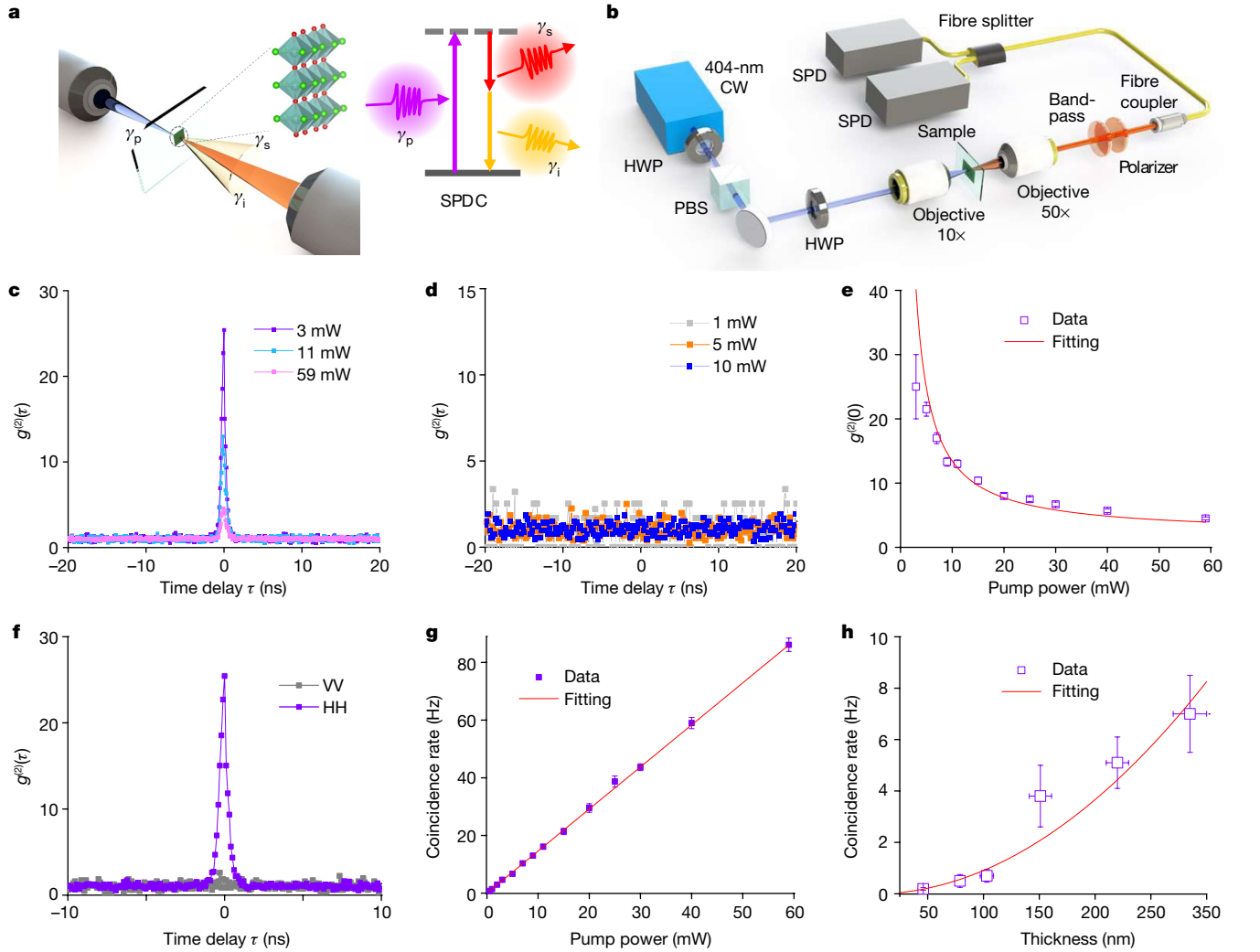

Fig. 4 | Nonclassical parametric photon pair generation through SPDC. **a**, Illustration of the SPDC process, in which a high-energy pump photon (γ_p) converts into a pair of low-energy photons consisting of a signal photon (γ_s) and an idler photon (γ_i). The $NbOCl_2$ flakes exfoliated on a sapphire substrate were used for measurements. **b**, Illustration of the optical setup for SPDC experiments. The band-pass filter centres at 810 nm with a 10 nm full-width at half-maximum. CW, continuous wave; PBS, polarizing beamsplitter; HWP, half-wave plate; SPD, single-photon detector. **c**,**d**, Normalized two-photon temporal correlation functions of the sample (**c**) and blank sapphire substrate (**d**) at different pump powers. **e**, Pump-power-dependent normalized correlation function at zero time delay. **f**, The normalized two-photon temporal correlation under different polarization configurations. The pump polarization is along the crystallographic *b* axis (denoted as H); HH (VV) indicates that the signal and idler photons are polarized parallel (perpendicular) to the pump. **g**, Pump-power-dependent coincidence rate. **h**, Thickness-dependent coincidence rate at a pump power of 3 mW. Error bars represent standard deviations from multiple measurements.

with other typical 2D layered materials (Supplementary Fig. 15). In addition, vibrational properties were also studied through Raman spectroscopy (Supplementary Section 4), and a thickness-insensitive and strongly in-plane anisotropic Raman response was observed (Supplementary Figs. 16–19). The Raman peak corresponding to mostly out-of-plane vibration also demonstrates a weak pressure and temperature dependence (Supplementary Fig. 20 and Supplementary Tables 2 and 3), implying unique interlayer vibrational properties.

SHG

The second-order NLO response of $NbOCl_2$ was investigated by SHG experiments under a back-reflection configuration (Fig. 3a). As shown in Fig. 3b, strong emission signals at half the corresponding excitation wavelengths were observed, with a quadratic excitation power dependence (Fig. 3c and Supplementary Figs. 21a–c), being a typical SHG process. The SHG intensity undergoes a slow increase when approaching a shorter wavelength and starts to become obvious from around 400 nm, which is consistent with the EELS results (Fig. 2a) and experimental optical absorption spectrum (Supplementary Fig. 10). Specifically, the SHG intensity increases with EELS intensity. This is because the EELS probability is intimately related to the local density of optical states[24], which dominates the transition rate from the two-photon excited state to the the ground state, and thus the SHG intensity[29,30]. As shown in Fig. 3b and Supplementary Fig. 21d, considerable resonance (enhancement) in SHG intensity can be observed when extending the wavelength from about 400 nm down to shorter wavelengths (that is, from about 3 eV to higher energy).

As shown in Fig. 3d, the SHG response is also highly in-plane anisotropic with a maximum response along the crystal polarization direction (*b* axis), which can be well explained and fitted on the basis of the crystal symmetry analysis (see details in Supplementary Section 5.2). Notably, the overall SHG intensity also exhibits a strong azimuthal dependence on excitation with a maximum along the *b* axis and a minimum along the *c* axis (Supplementary Fig. 22), due to low crystallographic symmetry, being basically different from

TMDCs whose overall SHG response shows no polarization dependence[29–31]. In particular, the high orthorhombic SHG contrast promises an easier crystallographic orientation identification and other polarization-related second-order nonlinear applications that are beyond the reach of TMDCs[13,31–35].

As the polar space group of bulk $NbOCl_2$ underpins a noncentrosymmetric character, along with the weak interlayer electronic coupling, we checked the layer-number-dependent SHG intensity. As shown in Fig. 3e,f, a positive scaling of SHG intensity with layer number, in a quadratic behaviour (within the penetration depth and coherence length, see Supplementary Section 5.3), is observed. Additional interference effects should be considered for the peaks and dips in Fig. 3h when the thickness is beyond the coherence length (see Supplementary Section 5.3 and Supplementary Figs. 23 and 24 for detailed analysis). As a comparison, we also measured the layer-dependent SHG intensity of WS_2, in which the SHG response exists only in odd layers and quickly decreases with layer number (Supplementary Fig. 25). Notably, a scalable and strong SHG intensity can be obtained in $NbOCl_2$ flakes, up to a level well beyond the reach of monolayer WS_2 (up to 10^{2-3} times; see Fig. 3f,h) although that of monolayer $NbOCl_2$ is relatively weaker (Supplementary Fig. 26). The effective second-order nonlinear coefficient (d_{eff}) was further calculated (Fig. 3g and Supplementary Section 5.4), and a layer-independent and high value of about 200 pm V^{-1} can be derived (for comparison with other second-order NLO materials, see Supplementary Section 5.4, Supplementary Table 4 and Supplementary Fig. 27). It is reasonable to expect that the strong and scalable second-order optical nonlinearity shall benefit from the vanishing interlayer electronic coupling and weak interlayer dielectric screening in addition to strong structural polarity. The monolayer-like d_{eff} is reminiscent of the monolayer-like excitonic effect, further evidencing the unique electronic and optical behaviours, in contrast to that of TMDCs (including 3R-MoS_2 and 2H-TMDC odd layers) in which evolving electronic structures and strong interlayer dielectric screening result in significant change in nonlinear susceptibilities[13,14].

Parametric photon pair generation

Ultracompact and integrable SPDC sources are under intense development for chip-based photonic quantum circuits but hindered by unavailable high-nonlinearity and integrable thin films[4,36–38]. The giant second-order optical nonlinearity in 2D layered $NbOCl_2$ stimulates us to explore it for a quantum light source. Accordingly, as illustrated in Fig. 4a,b, the SPDC process was first checked on a subwavelength $NbOCl_2$ flake (thickness of about 150 nm, exfoliated on a transparent sapphire substrate) with a continuous-wave laser at 404 nm. Photon pair generation was recorded by registering photon coincidences between two detectors[4,36]. The normalized second-order correlation functions $g^{(2)}(\tau)$ measured on the sample and blank substrate are presented in Fig. 4c,d, respectively, in which a peak at zero time delay means simultaneous arrival of one photon at each detector and thus is a signature of correlated photon pair generation. An obvious two-photon correlation peak with a peak-to-background ratio well above 2 at zero time delay ($g^{(2)}(0)$) was observed in the sample but not in the substrate, unambiguously demonstrating correlated photon pair generation through the SPDC process in the sample as the effects of thermal light bunching and substrate can be excluded[4,36,38]. In addition, the $g^{(2)}(0)$ value under different pumping power was also measured and exhibits an inverse pump power dependence (Fig. 4e), further evidencing a photon pair generation process. The polarization-dependent response (Fig. 4f) indicates the pump, signal and idler photons are all polarized along the crystallographic *b* axis. The pump-power-dependent photon pair coincidence rate was calculated from the data in Fig. 4e and follows a linear scaling relation (Fig. 4g), being a typical feature of the SPDC process (see Supplementary Section 6.2 for detailed analysis)[2,4,10]. Notably, with a pump power of 59 mW (available maximum power with our laser), a coincidence rate of about 86 Hz is detected. When the detection loss is considered, the actual value could be about 86 kHz with a figure of merit of 9,800 GHz W^{-1} m^{-1}, which is of great advantage for constructing on-chip SPDC sources (see Supplementary Section 6.1 and Supplementary Fig. 28 for detailed comparison and discussion)[10,21].

As shown in Fig. 4h, we also measured the SPDC response in flakes of different thicknesses, of which the coincidence rate increases with thickness following a quadratic relation as expected (see Supplementary Section 6.2 for detailed analysis)[2,10]. An SPDC response can be unambiguously observed in flakes as thin as 46 nm (corresponding normalized second-order correlation functions can be found in Supplementary Fig. 29), which, to the best of our knowledge, is the thinnest SPDC source that has ever been reported[2]. It is noteworthy that a higher coincidence rate could be obtained by optimizing the pump conditions (power and wavelength) and additional enhancement effects (for example, from resonant structures)[4,36], and consequently thinner SPDC sources might be expected.

Conclusion

In conclusion, we report a van der Waals crystal that exhibits vanishing interlayer electronic coupling and considerable monolayer-like excitonic behaviour in the bulk form, as well as strong and scalable second-order optical nonlinearity. The unprecedented second-order optical nonlinearity enables an SPDC process unambiguously observed in ultrathin van der Waals flakes, which bears great potential for applications in chip-based quantum light sources, as well as photon modulators and sensors[6,19,20]. In principle, the nonlinear efficiency can be further boosted by facile van der Waals integration with other nanophotonic structures such as low-loss metasurfaces, waveguides and cavities[5,20,37,38]. Moreover, $NbOX_2$ (X = Cl, Br and I) was recently predicted to simultaneously exhibit in-plane ferroelectricity and antiferroelectricity and associated phase transition between them[23], implying a potential electric control knob for the optical nonlinearity. Our results establish $NbOCl_2$ as a promising 2D layered material for integrated nonlinear photonics and optoelectronics.

As interlayer electronic coupling plays a vital role in shaping the properties of 2D materials—as particularly exemplified by the recently emerging twistronics that fundamentally results from interlayer coupling and hybridization effects[39,40]—this interlayer electronically decoupling system would be an interesting and complementary building block for atomic-scale Legos[5], and new physics and functionalities could be expected, in addition to the scalable optical nonlinearity reported in this work. On the other hand, the considerable and monolayer-like excitonic behaviour in the bulk form would open new playgrounds for exciton physics in 2D layered systems.

Online content

Any methods, additional references, Nature Portfolio reporting summaries, source data, extended data, supplementary information, acknowledgements, peer review information; details of author contributions and competing interests; and statements of data and code availability are available at https://doi.org/10.1038/s41586-022-05393-7.

1. Elshaari, A. W., Pernice, W., Srinivasan, K., Benson, O. & Zwiller, V. Hybrid integrated quantum photonic circuits. *Nat. Photon.* **14**, 285–298 (2020).
2. Wang, Y., Jöns, K. D. & Sun, Z. Integrated photon-pair sources with nonlinear optics. *Appl. Phys. Rev.* **8**, 011314 (2021).
3. Li, L. et al. Metalens-array–based high-dimensional and multiphoton quantum source. *Science* **368**, 1487–1490 (2020).
4. Santiago-Cruz, T., Sultanov, V., Zhang, H., Krivitsky, L. A. & Chekhova, M. V. Entangled photons from subwavelength nonlinear films. *Opt. Lett.* **46**, 653–656 (2021).
5. Liu, Y., Huang, Y. & Duan, X. Van der Waals integration before and beyond two-dimensional materials. *Nature* **567**, 323–333 (2019).

6. Hong, H. et al. Giant enhancement of optical nonlinearity in two-dimensional materials by multiphoton-excitation resonance energy transfer from quantum dots. *Nat. Photon.* **15**, 510–515 (2021).
7. Wang, G. et al. Giant enhancement of the optical second-harmonic emission of WSe_2 monolayers by laser excitation at exciton resonances. *Phys. Rev. Lett.* **114**, 097403 (2015).
8. Shi, J. et al. 3R MoS_2 with broken inversion symmetry: a promising ultrathin nonlinear optical device. *Adv. Mater.* **29**, 1701486 (2017).
9. Adelwahab, I. et al. Giant second-harmonic generation in ferroelectric $NbOI_2$. *Nat. Photon.* **16**, 644–650 (2022).
10. Marini, L., Helt, L. G., Lu, Y., Eggleton, B. J. & Palomba, S. Constraints on downconversion in atomically thick films. *J. Opt. Soc. Am. B* **35**, 672 (2018).
11. Dinparasti Saleh, H. et al. Towards spontaneous parametric down conversion from monolayer MoS_2. *Sci. Rep.* **8**, 3862 (2018).
12. Kumar, N. et al. Second harmonic microscopy of monolayer MoS_2. *Phys. Rev. B* **87**, 161403 (2013).
13. Li, Y. et al. Probing symmetry properties of few-layer MoS_2 and h-BN by optical second-harmonic generation. *Nano Lett.* **13**, 3329–3333 (2013).
14. Le, C. T. et al. Effects of interlayer coupling and band offset on second harmonic generation in vertical $MoS_2/MoS_{2(1-x)}Se_{2x}$ structures. *ACS Nano* **14**, 4366–4373 (2020).
15. Zhang, J., Zhao, W., Yu, P., Yang, G. & Liu, Z. Second harmonic generation in 2D layered materials. *2D Mater.* **7**, 042002 (2020).
16. Yu, J. et al. Giant nonlinear optical activity in two-dimensional palladium diselenide. *Nat. Commun.* **12**, 1083 (2021).
17. Song, Y. et al. Extraordinary second harmonic generation in ReS_2 atomic crystals. *ACS Photon.* **5**, 3485–3491 (2018).
18. Hu, L. & Huang, X. Peculiar electronic, strong in-plane and out-of-plane second harmonic generation and piezoelectric properties of atom-thick α-M_2X_3 (M = Ga, In; X = S, Se): role of spontaneous electric dipole orientations. *RSC Adv.* **7**, 55034–55043 (2017).
19. Leuthold, J., Koos, C. & Freude, W. Nonlinear silicon photonics. *Nat. Photon.* **4**, 535–544 (2010).
20. Datta, I. et al. Low-loss composite photonic platform based on 2D semiconductor monolayers. *Nat. Photon.* **14**, 256–262 (2020).
21. Marino, G. et al. Spontaneous photon-pair generation from a dielectric nanoantenna. *Optica* **6**, 1416 (2019).
22. Hillebrecht, H. et al. Structural and scanning microscopy studies of layered compounds MCl_3 (M = Mo, Ru, Cr) and $MOCl_2$ (M =V, Nb, Mo, Ru, Os). *J. Alloys Compd.* **246**, 70–79 (1997).
23. Jia, Y., Zhao, M., Gou, G., Zeng, X. C. & Li, J. Niobium oxide dihalides $NbOX_2$: a new family of two-dimensional van der Waals layered materials with intrinsic ferroelectricity and antiferroelectricity. *Nanoscale Horiz.* **4**, 1113–1123 (2019).
24. Polman, A., Kociak, M. & Garcia de Abajo, F. J. Electron-beam spectroscopy for nanophotonics. *Nat. Mater.* **18**, 1158–1171 (2019).
25. Li, L. et al. Direct observation of the layer-dependent electronic structure in phosphorene. *Nat. Nanotechnol.* **12**, 21–25 (2017).
26. Yang, Y. et al. Weak interlayer interaction in 2D anisotropic $GeSe_2$. *Adv. Sci.* **6**, 1801810 (2019).
27. Garza, A. J. & Scuseria, G. E. Predicting band gaps with hybrid density functionals. *J. Phys. Chem. Lett.* **7**, 4165–4170 (2016).
28. Wang, X., Meng, W. & Yan, Y. Electronic band structures and excitonic properties of delafossites: a GW-BSE study. *J. Appl. Phys.* **122**, 085104 (2017).
29. Zhou, X. et al. Strong second-harmonic generation in atomic layered GaSe. *J. Am. Chem. Soc.* **137**, 7994–7997 (2015).
30. Yao, K. et al. Continuous wave sum frequency generation and imaging of monolayer and heterobilayer two-dimensional semiconductors. *ACS Nano* **14**, 708–714 (2020).
31. Wang, Y., Xiao, J., Yang, S., Wang, Y. & Zhang, X. Second harmonic generation spectroscopy on two-dimensional materials [Invited]. *Opt. Mater. Express* **9**, 1136–1149 (2019).
32. Wu, Q., Hewitt, T. D. & Zhang, X.-C. Two-dimensional electro-optic imaging of THz beams. *Appl. Phys. Lett.* **69**, 1026–1028 (1996).
33. Platonov, A. V., Kochereshko, V. P., Ivchenko, E. L. & Mikhailov, G. V. Giant electro-optical anisotropy in type-II heterostructures. *Phys. Rev. Lett.* **83**, 3546–3549 (1999).
34. Ribeiro-Soares, J. et al. Second harmonic generation in WSe_2. *2D Mater.* **2**, 045015 (2015).
35. Autere, A. et al. Nonlinear optics with 2D layered materials. *Adv. Mater.* **30**, 1705963 (2018).
36. Okoth, C., Cavanna, A., Santiago-Cruz, T. & Chekhova, M. V. Microscale generation of entangled photons without momentum conservation. *Phys. Rev. Lett.* **123**, 263602 (2019).
37. Trovatello, C. et al. Optical parametric amplification by monolayer transition metal dichalcogenides. *Nat. Photon.* **15**, 6–10 (2020).
38. Santiago-Cruz, T. et al. Photon pairs from resonant metasurfaces. *Nano Lett.* **21**, 4423–4429 (2021).
39. Hu, G. et al. Topological polaritons and photonic magic angles in twisted α-MoO_3 bilayers. *Nature* **582**, 209–213 (2020).
40. Andrei, E. Y. & MacDonald, A. H. Graphene bilayers with a twist. *Nat. Mater.* **19**, 1265–1275 (2020).

Methods

Crystal synthesis

Bulk single crystals were synthesized by chemical vapour transport[22]. Chemical powders (Nb_2O_5, 4N, Alfa Aesar; $NbCl_5$, 5N, Alfa Aesar; Nb, 3N, Sinopharm Chemical Reagent Co.) in stoichiometric ratio were first thoroughly mixed and sealed in an evacuated quartz tube (about 20 cm long) under vacuum of 10^{-6} torr. The sealed tube was then heated in a two-zone furnace, with the reaction region kept at 500–600 °C and the growth region kept at 300–400 °C for 5 days, followed by slow cooling to room temperature at a rate of about 5 °C h^{-1}. Finally single crystals (rectangle-shaped thin plates) were obtained at the growth region.

Characterization

X-ray diffraction was conducted on a Rigaku D/MAX 2550/PC with Cu Kα X-rays. Atomic force microscopy measurements were performed on a Bruker Dimension FastScan in tapping mode. Cross-sectional STEM images and core-loss EELS mapping images were acquired at 80 kV using a JEOL ARM200F equipped with a CEOS ASCOR hexapole aberration corrector, a cold field-emission gun and a Gatan Quantum ER spectrometer. During the imaging process, the probe size, probe-forming aperture, camera length and inner angle of the high-angle annular dark-field detector were selected as 8C, 31 mrad, 8 cm and 81 mrad, respectively. During core-loss EELS measurements, the energy dispersion, probe size and camera length were selected as 0.1 eV per channel, 6C and 4 cm, respectively. The full-width at half-maximum of the zero-loss peak is 1.3 eV. The atomic in-plane $NbOCl_2$ structure was probed by an aberration-corrected Nion U-HERMES100 at 60 kV. The convergence semi-angle is 32 mrad, and the collection semi-angle spans from 75 to 210 mrad for the high-angle annular dark field. For the valence EELS measurements, 21 meV full-width at half-maximum of the zero-loss peak was achieved with 3 meV per channel dispersion. The exposure time for a single frame is 600–800 ms. To optimize the signal-to-noise ratio, each experimental valence EEL spectrum was obtained by integrating around 400 frames. Following the same experimental parameters, an EEL spectrum was collected in vacuum to eliminate the long-range coupling effects. EELS data were processed by the Digital Micrograph and open-source HyperSpy software programs. Background subtraction for all of the valence EEL spectra was performed by fitting a power-law function with an identical fitting window from 1.42 to 1.62 eV. Spike noise in the spectra was removed by a total variation denoising strategy in HyperSpy[41]. The optical excitation onset energy was then extracted through fitting the onset region of EELS by the tangent method. The samples were all-dry transferred onto holey silicon nitride support film (PELCO, Ted Pella) for STEM characterization.

Raman spectra were conducted on a commercial WITec Raman system with a 532-nm excitation laser, except that polarized Raman spectra were measured on an NT-MDT confocal spectroscopy system, in which the linear-polarized laser (532 nm) is focused by a 100× objective lens with a numerical aperture (NA) of 0.9, and an analyser in front of the entrance of the spectrometer is used to perform parallel or perpendicular measurements. For temperature-dependent Raman spectra, the sample was loaded in a liquid-helium-cooled Oxford chamber. The pressure-dependent Raman spectroscopy was performed at room temperature on a Renishaw Raman spectrometer (RM1000) with a 532-nm excitation laser. The Raman system was calibrated by the Si line before measurements, and a laser beam of about 10 μm in diameter was focused at the chosen location of the samples in the diamond anvil cell. Pressure was determined by measuring the ruby fluorescence[42].

SHG experiment

The SHG experiments were conducted on a home-built optical system operated in reflection geometry. A tunable femtosecond laser (pulse width: 180 fs; repetition frequency: 80 MHz) was used as the excitation source, which passes through a polarizing beamsplitter, an 808-nm half-wave plate, a dichroic mirror and an objective (100×, NA 0.9) before interaction with samples. The same objective was used to collect the SHG signal, which was then passed through a short-pass filter (centred at 780 nm) and a 405-nm band-pass filter (centred at 405 nm with a full-width at half-maximum of 10 nm) in sequence. A multimode fibre was then used to collect and guide the signal into a single-photon detector (Excelitas Technologies, single-photon counting module, SPCM-800-14-FC). The spectrum was measured using a spectrometer (Princeton Instruments, SP2500) cooled by liquid nitrogen. All of the experiments were carried out at room temperature. Polarized excitation was realized by an 808-nm half-wave plate in the excitation path, and SHG polarization was analysed by a 404-nm half-wave plate and a polarizing beamsplitter in the collection path.

Nonclassical parametric photon pair generation

The two-photon correlation properties were recorded by registering photon coincidences between two single-photon detectors (same as used in SHG experiments) at the two outputs of a fibre beamsplitter (Fig. 4b). A 404-nm continuous-wave laser (Diode Laser, Toptica Photonics) was used to pump the parametric down-conversion processes. The pump laser passed through a polarizing beamsplitter and two 404-nm half-wave plates, the first of which was used for adjusting the laser power and the other was used for polarization control. Then the pump laser was focused on the sample through an objective (10×, NA 0.3). We used an objective (50×, NA 0.42) to collect the signals. The signals passed through a band-pass filter (centred at 810 nm with a full-width at half-maximum of 10 nm) and a polarizer (Thorlabs, LPVIS100-MP2), before coupling into a multimode fibre. We used a fibre beamsplitter (50/50) to divide the signal into two paths, followed by detection with two single-photon detectors respectively. Finally, the coincidence was determined by measuring correlations between the two detectors.

Density functional theory calculations

The *GW* calculations were carried out using the Vienna Ab initio Simulations Package (VASP-6.2.1)[43] at the G_0W_0 level, in which many-body interactions were included to obtain the quasiparticle electronic features. The quasiparticle energies were adopted to obtain the band structures by Wannier interpolation though the Wannier90 program. The valence electrons were treated explicitly, and core electrons were represented with projector augmented wave potentials. The Kohn–Sham equations were solved self-consistently with a plane-wave basis set with periodic boundary conditions. The exciton energy levels and absorption spectra were calculated through solving the Bethe–Salpeter equation including the *e*–*h* interactions, on the basis of the G_0W_0 results. The matrices were used to incorporate excitons in the calculations. The Heyd–Scuseria–Ernzerhof[44,45] hybrid functional calculations were conducted using the projector augmented wave method as implemented in the Vienna Ab initio Simulation Package (VASP) 5.4.4 code[43]. The plane-wave cutoff energy was set to 500 eV. Γ-centred *k*-meshes with *k*-spacing of 0.2 $Å^{-1}$ and 1 × 6 × 4 Monkhorst–Pack *k*-meshes were used for the bulk and monolayer $NbOCl_2$ (the bulk form has a *C*2 monoclinic symmetry whereas the monolayer form has a *Pmm*2 orthorhombic symmetry), respectively. All of the structure calculations were performed using the generalized gradient approximation Perdew–Burke–Ernzerhof functional[46] as the exchange–correlation functional, and the crystal structures were fully relaxed until the total force on each atom was <0.01 eV $Å^{-1}$. To remedy the underestimation of the bandgaps in Perdew–Burke–Ernzerhof methods, the electronic structure and optical calculations for bulk and monolayer $NbOCl_2$ were performed using the Heyd–Scuseria–Ernzerhof[44,45] hybrid functional. The transition matrix elements were calculated using VASP_TDM code[47]. For the calculation of interlayer charge density and binding, cleavage and translation energies, the pseudopotential for Nb was constructed treating the semi-core *s* states as valence states. The electronic wavefunctions were

represented in a plane-wave basis set with an energy cutoff 400 eV. The 2D $NbOCl_2$ layer is modelled as a slab with a vacuum region of more than 20 Å along the out-of-plane *a* direction. The *k*-point sampling is $2 \times 6 \times 4$ for the bulk form and $1 \times 6 \times 2$ for the monolayer form. The total energy was converged numerically to less than 10^{-5} meV per atom with respect to electronic, ionic and unit-cell degrees of freedom.

The density functional theory calculations of Raman spectra were performed using the norm-conserving pseudopotential method as implemented in the Quantum Espresso package[48]. The exchange-correlation potentials were treated using the local density approximation[49]. The pseudopotentials were obtained using the Pseudo Dojo Potentials[50,51]. Before the Raman spectra calculations, the structure was optimized until the convergence threshold on energy was 1.0×10^{-8} Ry. A kinetic energy cutoff of 50 Ry for wavefunctions and $6 \times 6 \times 4$ Monkhorst–Pack *k*-meshes were used for energy convergence. The phonon and Raman spectra were calculated within density functional perturbation theory as introduced previously[52]. For the self-consistent iteration of the density functional perturbation theory, a kinetic energy cutoff of 50 Ry and a convergence threshold of 1.0×10^{-14} Ry were used.

Data availability

All data supporting the findings of this study are available in the main text, Methods or Supplementary Information. The data are also available from the corresponding authors upon reasonable request.

41. Peña, F. D. L. et al. hyperspy/hyperspy: release v1.6.5 (v1.6.5). *Zenodo* https://doi.org/10.5281/zenodo.5608741 (2021).
42. Mao, H. K., Xu, J. & Bell, P. M. Calibration of the ruby pressure gauge to 800 kbar under quasihydrostatic conditions. *J. Geophys. Res.* **91**, 4673–4676 (1986).
43. Kresse, G., Furthmüller, J., Furthmuller, J. & Furthmüller, J. Efficient iterative schemes for ab initio total-energy calculations using a plane-wave basis set. *Phys. Rev. B* **54**, 11169–11186 (1996).
44. Heyd, J., Scuseria, G. E. & Ernzerhof, M. Hybrid functionals based on a screened coulomb potential. *J. Chem. Phys.* **118**, 8207–8215 (2003).
45. Peralta, J. E., Heyd, J., Scuseria, G. E. & Martin, R. L. Spin-orbit splittings and energy band gaps calculated with the Heyd-Scuseria-Ernzerhof screened hybrid functional. *Phys. Rev. B* **74**, 073101 (2006).
46. Perdew, J. P., Burke, K. & Ernzerhof, M. Generalized gradient approximation made simple. *Phys. Rev. Lett.* **77**, 3865–3868 (1996).
47. VASP_TDM *GitHub* https://github.com/QijingZheng/VASP_TDM (2016).
48. Giannozzi, P. et al. QUANTUM ESPRESSO: a modular and open-source software project for quantum simulations of materials. *J. Phys. Condens. Matter* **21**, 395502 (2009).
49. Perdew, J. P. & Zunger, A. Self-interaction correction to density-functional approximations for many-electron systems. *Phys. Rev. B* **23**, 5048–5079 (1981).
50. van Setten, M. J. et al. The PseudoDojo: training and grading a 85 element optimized norm-conserving pseudopotential table. *Comput. Phys. Commun.* **226**, 39–54 (2018).
51. Hamann, D. R. Optimized norm-conserving Vanderbilt pseudopotentials. *Phys. Rev. B* **88**, 085117 (2013).
52. Lazzeri, M. & Mauri, F. First-principles calculation of vibrational Raman spectra in large systems: signature of small rings in crystalline SiO_2. *Phys. Rev. Lett.* **90**, 036401 (2003).

Acknowledgements Q.G., S.J.P. and A.T.S.W. acknowledge financial support from the Ministry of Education Tier 2 grant MOE2017-T2-2-139. Q.G. sincerely thanks Q. Zhang, K. Zheng and G. Xu for help with chemicals and furnace facilities for crystal synthesis and X-ray diffraction measurements. Q.G. sincerely thanks M. Li for valuable discussions. Q.G. thanks M. Wu, Y. Yu and J. Dan for help with STEM. X.-F.R. and G.-C.G. acknowledge financial support of the Innovation Program for Quantum Science and Technology (grant number 2021ZD0303200), the National Natural Science Foundation of China (grant numbers 61590932, 11774333, 62061160487 and 12004373), the Anhui Initiative in Quantum Information Technologies (grant number AHY130300) and the Strategic Priority Research Program of the Chinese Academy of Sciences (grant number XDB24030601). This work was partially carried out at the USTC Center for Micro and Nanoscale Research and Fabrication. The work at University of Chinese Academy of Sciences was financially supported by the National Key R&D Program of China (2018YFA0305800) and the Beijing Outstanding Young Scientist Program (BJJWZYJH012019144300039). C.-W.Q. acknowledges the financial support of the National Research Foundation, Prime Minister's Office, Singapore under Competitive Research Program Award NRF-CRP26-2021-0004. H.G. acknowledges the financial support of the National Science Fund for Distinguished Young Scholars (grant number T2225027). Z.X. acknowledges the financial support of the National National Science Foundation of China (grant number 51972130). X.Z. acknowledges the financial support of the Peking University startup funding and the National Natural Science Foundation of China (grant number 52273279).

Author contributions Q.G. conceived the ideas, designed the experiments and organized the research project under the supervision of A.T.S.W., S.J.P. and C.-W.Q. Q.G. synthesized the crystals and prepared all samples for the experiments. Q.G., J.W., B.Y., Wenju Zhou, G.E. and H.G. measured Raman spectra. M.G., W. Zang., X.Z., M.X., Wu Zhou and S.J.P. carried out STEM-related characterization techniques. X.-Z.Q., Q.G., Y.-K.W., X.-F.R. and G.-C.G. designed and conducted the harmonic generation and parametric down-conversion experiments. S.H., L.Z., Z.X. and Y.P.F. carried out the theoretical calculations. S.A.Y. provided theoretical support in revision. Q.G. analysed the data and drafted the manuscript with input from all authors. Q.G., C.-W.Q., X.-F.R., S.J.P. and A.T.S.W. provided major revisions. All authors discussed the results and contributed to the manuscript.

Competing interests The authors declare no competing interests.

Additional information

Supplementary information The online version contains supplementary material available at https://doi.org/10.1038/s41586-022-05393-7

Correspondence and requests for materials should be addressed to Qiangbing Guo, Xi-Feng Ren, Cheng-Wei Qiu, Stephen J. Pennycook or Andrew T. S. Wee.

Peer review information *Nature* thanks Daniele Faccio, Gaoyang Gou and the other, anonymous, reviewer(s) for their contribution to the peer review of this work.